

Full Length Article

Doping strategy on properties and chemical mechanical polishing performance of CeO₂ Abrasives: A DFT assisted experimental studyJiahui Ma ^{a,b}, Ning Xu ^{a,b,c,d,*}, Jinrong Hu ^e, Yuxin Luo ^{a,b}, Yu Lin ^{a,b}, Yongping Pu ^{a,b}^a School of Material Science and Engineering, Shaanxi University of Science & Technology, Xi'an, Shaanxi Province 710021, China^b Shaanxi Key Laboratory of Green Preparation and Functionalization for Inorganic Materials, Xi'an, Shaanxi Province 710021, China^c Key Laboratory of Auxiliary Chemistry and Technology for Chemical Industry, Ministry of Education, Shaanxi University of Science and Technology, Xi'an, Shaanxi Province 710021, China^d Shaanxi Collaborative Innovation Center of Industrial Auxiliary Chemistry and Technology, Shaanxi University of Science and Technology, Xi'an, Shaanxi Province 710021, China^e State Key Laboratory of Advanced Technology for Materials and Processing, Wuhan University of Technology, Wuhan, Hubei Province 430070, China

ARTICLE INFO

ABSTRACT

Keywords:

CeO₂ abrasives
Density functional theory (DFT)
Vacancy formation energy (E_{vac})
Chemical mechanical polishing (CMP)
Removal mechanism

A series of Ce_{1-x}M_xO₂ abrasives with different types and amounts of doping were prepared by molten salt method. The properties of abrasives were characterized in detail by XRD, SEM, EDS and XPS. For all doping types, the morphology of abrasives changes from spherical to octahedral and their size decreases continuously with the doping increases. The Ce³⁺ concentration on the CeO₂ abrasive surface is also increased by doping. The density functional theory indicates the vacancy formation energy of CeO₂ systems are reduced by doping. The mechanism of transition from Ce⁴⁺ to Ce³⁺ induced in CeO₂ system by doping is also discussed. CMP experiments show that the efficiency of the abrasives is significantly enhanced by doping. The MRR of Y³⁺, La³⁺ and Pr³⁺ doped CeO₂ abrasives increased by 56 %, 40 % and 44 % compared with the pure. It is also shown that the appropriate amount ($x = 0.08$) should be considered in order to obtain excellent performance. It is confirmed that the substrate surface with almost no damage and low roughness is obtained after polishing. The removal mechanism of CeO₂ abrasives on SiO₂ substrate is comprehensively analyzed by considering the size, morphology and defects of the abrasives.

1. Introduction

Chemical mechanical polishing (CMP) [1–4] is the flattening technique that takes into account both local and global aspects of materials, which achieves the microscale removal of materials through the synergy of surface chemical reactions and mechanical grinding [5]. CMP is known as a “black box” technology, a large number of practical experience has shown that the slurry and the abrasives in it are the key factors affecting the CMP performance [6]. In particular, the key CeO₂ abrasives are widely used for CMP processing in the industries of optical lens and semiconductor [7]. The micromorphology, particle size, mechanical properties, crystal structure and defects of CeO₂ abrasives are considered to have direct impacts on the removal rate and surface quality of materials [8]. Kim et al. [9] believed that abrasives with sharp edges have a better polishing performance than those with spherical on the initial surface with large bumps and depressions. Based on the

contact area model, Yang et al. [10] found that spherical CeO₂ abrasives with smaller size had better removal result on serrated edges due to the increase of the total contact area with the substrate. From the perspective of mechanical contact between the abrasives and the substrate, a number of researchers also designed a series of core/shell structure composite abrasives. Chen et al. [11–13] designed PS/CeO₂, PMMA/CeO₂ and SiO₂/CeO₂ composite abrasives. It is believed that the spring effect of organic core can effectively adjust the contact state between the abrasives and the workpiece, which reduces the damage of the hard abrasives to the materials. Peedikakkandy et al. [14] designed SiO₂/CeO₂ composite abrasives with stable structure and found that it had good selectivity for the polishing between SiO₂ and Si₃N₄ substrates. However, the MRR of the abrasives is generally low, and the shell is prone to structural and functional failure under the load, which limits its application in the semiconductor industry where linewidth requirements are getting smaller and smaller.

* Corresponding author at: School of Material Science and Engineering, Shaanxi University of Science & Technology, Xi'an, Shaanxi Province 710021, China.
E-mail address: xuning@sust.edu.cn (N. Xu).

The evolution of integrated circuit technology has brought a rapid growth in the demand for polishing materials, which requires the improvement of polishing efficiency. Sabia and Stevens [15] found that there is not only Ce⁴⁺ but also a certain amount of Ce³⁺ on the surface of CeO₂ abrasives during the polishing. Seo et al. [16] confirmed that the polishing efficiency of the CeO₂ abrasives is enhanced by improving its proportion of Ce³⁺. Schmitt et al. [17] considered that the doping of trivalent ions is more favorable than others for the formation of Ce³⁺ on CeO₂ crystals. Patil et al. [18] also found that the doping of trivalent ions would generate a large number of oxygen vacancies, but it would not have a significant effect on the structure of CeO₂ crystal. Cheng et al. [19] doped lanthanides (La, Nd, Yb) into the surface of commercial CeO₂ abrasives, and the polishing efficiency of the abrasives on the SiO₂ substrate was significantly improved. Kim et al. [20] also reported that the MRR of CeO₂ abrasives with high concentration Nd³⁺ doping was improved by 3.62 times compared with the pure groups. Generally, the improvement of CMP performance by the Ce³⁺ on CeO₂ abrasives has been experimentally verified, and the abrasives have been modified by doping. However, the effects of different types and amounts of doping on crystal structure, micromorphology and defects of CeO₂ abrasives need to be further understood. The complexity and the mechanism of defect formation have not been elucidated in detail. Furthermore, the influence of a series of changes in abrasives caused by doping on CMP performance has not been comprehensively analyzed.

In this work, a series of Ce_{1-x}M_xO₂ abrasives with different types (M = Y, La, Pr) and amounts ($x = 0.00, 0.02, 0.04, 0.06, 0.08, 0.10$) of doping were prepared by a simple molten salt method. The effects of different types and amounts of doping on the crystal structure, micromorphology and defects of CeO₂ abrasives were investigated. The defects in CeO₂ crystal are analyzed by theoretical calculation and experimental characterization, and the mechanism of the transformation from Ce⁴⁺ to Ce³⁺ induced by doping is explained. In addition, the influence of the change of particle size, morphology and defects of the abrasives caused by doping on the CMP performance is discussed. And the CMP mechanism of CeO₂ abrasives is also discussed in detail. To the best of our knowledge, a detailed explanation of the effect of doping on the properties of CeO₂ abrasives and its CMP performance on SiO₂ substrates has not been reported so far.

2. Experiment

2.1. Chemicals and reagents

Cerium nitrate hexahydrate (Ce(NO₃)₃·6H₂O), Lanthanum nitrate hydrate (La(NO₃)₃·nH₂O), Praseodymium nitrate hydrate (Pr(NO₃)₃·6H₂O), Yttrium nitrate hexahydrate (Y(NO₃)₃·6H₂O)), Potassium Chloride (KCl), Sodium chloride (NaCl) are all analytical reagent, they are all purchased from Sinopharm Chemical Reagent Co., Ltd. (China). Analytical reagent ethanol is purchased from Tianjin Fuyu Fine Chemical Co., Ltd. (China). Homemade deionized water is used throughout the experiment. All chemicals are used without further purification.

2.2. Preparation of Ce_{1-x}M_xO₂ abrasives

A series of Ce_{1-x}M_xO₂ (M = La, Pr, Y; $x = 0.00, 0.02, 0.04, 0.06, 0.08, 0.10$) abrasives were prepared by a simple molten salt method. A typical synthesis [21] is described as follows: high-purity cerium nitrate, lanthanum nitrate, praseodymium nitrate and yttrium nitrate were used as precursors for the preparation of Ce_{1-x}M_xO₂ particles. Firstly, according to the stoichiometric weights, the precursor was weighed in a total molar amount of 5 mmol, and the KCl-NaCl eutectic salt (a molar ratio of 1:1, the eutectic point was 657 °C) was weighed in a molar ratio of 1:10. Next, the precursor and eutectic salt were ground separately and the raw materials were mixed in absolute ethanol. The mixture was transferred to an alumina porcelain boat and dried in an oven at 80 °C.

Then, it was calcined in a muffle furnace with a certain temperature regime to obtain a mixture containing CeO₂ particles. Finally, the impurity salts in the mixture were washed away with hot deionized water to obtain high-purity Ce_{1-x}M_xO₂ particles.

2.3. Characterization of the abrasives

The phase and crystal structure of all abrasives was analyzed using X-ray diffraction (XRD, D8 Advance, Bruker, Germany) with Cu K α radiation ($\lambda = 0.15418$ nm) from 20° to 80° at a rate of 0.02° s⁻¹. The micromorphology and elemental distribution of the abrasives were characterized by scanning electron microscopy (SEM, Apreo S, FEI, USA) equipped with an energy dispersive spectrometers (EDS). The chemical states of elements were analyzed by an X-ray photoelectron spectroscope (XPS, Thermo Scientific K-Alpha, USA) with a monochromatized Al K α source, and the pass energy was set to be 100.0 eV for the survey scan and 50.0 eV for the fine scan. The binding energy was calibrated using the adsorbed carbon (284.8 eV) as the energy standard.

2.4. Density functional theory (DFT) calculation

All structural relaxation and total energy calculations were performed with the density functional theory (DFT) method [22], as implemented in the Vienna Ab initio Simulation Package (VASP) [23,24]. The projector augmented wave (PAW) method was utilized to describe the electron-ion interaction. The exchange-correlation interaction functional is the generalized gradient approximation (GGA) in the Perdew-Burke-Ernzerhof (PBE) functional [22,25] and the electron wave functions are expanded using the plane waves with an energy cutoff of 500 eV [19]. In this calculation, the U parameter applied to the Ce4f and O2p states were set to 5 and 5.5 eV, respectively [19,26]. The convergence of total energy and the force between atoms were set to 10⁻⁵ eV and 0.01 eV·Å⁻¹, respectively. The G-centered Monkhorst-Pack k-mesh with a size of 2 × 2 × 2 was applied [19]. All atomic positions were fully relaxed by using of conjugate gradient algorithm.

2.5. CMP experiment

These CMP slurries were simply prepared for polishing tests. The abrasives was dispersed by ball milling, the solid content of the slurries was adjusted to 0.5 wt%, and the pH of the slurries was adjusted to 6.0 using low-concentration ammonia and nitric acid solution. All slurries were homogenized using a magnetic stirrer before the CMP test. The quartz glass with a nominal diameter of 20 mm and a thickness of 2 mm purchased from Lianyungang Xiongtai Quartz Technology Co., Ltd. (China) was used as the material to be polished. The CMP experiments were performed on UNIPOL-1200S automatic pressure grinding and polishing machine (Shenyang Kejing Auto-instrument, Co. LTD, China) equipped with synthetic leather polishing pad (Shenyang Kejing Auto-instrument, Co. LTD, China). Then the detailed polishing parameters are described as follows: the rotation speed of the platen and the carrier were both 80 r/min, the self-rotation direction was opposite, the applied polishing load was 3.5 kg, the polishing time was 3 min, and the slurry supplying rate was 25 mL/min.

The polished samples were repeatedly cleaned by ultrasonic waves in deionized water, and CMP performance was characterized after the glass was dried. Surface defects and roughness of the substrate were characterized by atomic force microscopy (AFM, Seiko SPA400-SP13800N, Japan) equipped with a silicon nitride tip, which was scanned over a 5 μm × 5 μm area in contact mode at a rate of 1.0 Hz. In the evaluation of polishing efficiency, a precision electronic balance with an accuracy of 0.1 mg was used to measure the weight of the polished workpiece. The MRR was obtained by indirect calculation through Eq. (1) [27,28].

$$MRR = \frac{m_0 - m}{\rho \times S \times t} \quad (1)$$

where m_0 and m are the mass of the quartz substrate before and after polishing, respectively, ρ is the nominal density of commercial quartz glass (2.2 g/cm^3), S is the area of the substrate ($\pi \text{ cm}^2$), and t is the polishing time (3 min). In the CMP test, all MRR and roughness data presented are based on the average of three replicated experiments.

3. Results and discussion

3.1. Phase analysis

The XRD pattern of $\text{Ce}_{1-x}\text{Y}_x\text{O}_2$ abrasives ($x = 0.00, 0.02, 0.04, 0.06, 0.08, 0.10$) is shown in Fig. S1. The diffraction peaks appear at 2θ about $28.5^\circ, 33.1^\circ, 47.5^\circ, 56.3^\circ, 59.1^\circ, 69.4^\circ, 76.7^\circ$ and 79.1° , which are attributed to the (111), (200), (220), (311), (222), (400), (331) and (420) planes of the CeO_2 phase (PDF#34–0394) with cubic fluorite structure, respectively. Moreover, no other impurity phases (Y_2O_3 , etc.) were identified with the increase of Y^{3+} doping, which indicates the formation of Ce-Y-O solid solution in all samples. It is also noted that the peak position shifts to a lower angle with the increase of Y^{3+} doping. The lattice expansion of CeO_2 results in a shift in the trend of the peaks [29], which is attributed to the fact that the radius of Y^{3+} (90 pm) is larger than that of Ce^{4+} (87 pm). The XRD patterns of a series of $\text{Ce}_{1-x}\text{La}_x\text{O}_2$ and $\text{Ce}_{1-x}\text{Pr}_x\text{O}_2$ abrasives prepared also showed a similar trend, as shown in Fig. S1(a) and Fig. S2 (a). Differently, the deviation degree and full width at half maxima (FWHM) of the peaks are controlled by ion radius.

The influence of doping on CeO_2 phase was analyzed by GSAS program, the Rietveld refinement results based on the XRD patterns of $\text{Ce}_{1-x}\text{Y}_x\text{O}_2$ samples are shown in Fig. 1. The red circle represents the recorded, the black line marks the calculated, and the blue line shows the different profiles for the CeO_2 powder in the Figs. All the refinements were running to low refinement parameters ($R_p < 6\%$, $R_{wp} < 8\%$, $\chi^2 < 2$), which ensures that the result are credible. Table 1 shows the Rietveld refinement results of lattice parameters and unit cell volume of the $\text{Ce}_{1-x}\text{Y}_x\text{O}_2$ samples. The results show that the lattice constant and cell volume of CeO_2 crystal are continuously increased with the incorporation of Y^{3+} , which is consistent with the results of the XRD patterns.

Table 1

The Rietveld refinement results of lattice constant and unit cell volume of the $\text{Ce}_{1-x}\text{Y}_x\text{O}_2$ samples.

Type	Lattice constant (Å)	Lattice volume (Å ³)
Pure CeO_2	5.4113(61)	158.5(52)
$\text{Ce}_{0.98}\text{Y}_{0.02}\text{O}_2$	5.4119(48)	158.5(11)
$\text{Ce}_{0.96}\text{Y}_{0.04}\text{O}_2$	5.4119(69)	158.5(13)
$\text{Ce}_{0.94}\text{Y}_{0.06}\text{O}_2$	5.4121(25)	158.5(27)
$\text{Ce}_{0.92}\text{Y}_{0.08}\text{O}_2$	5.4124(04)	158.5(52)
$\text{Ce}_{0.9}\text{Y}_{0.1}\text{O}_2$	5.4133(18)	158.6(32)

3.2. Characterization of morphology

The morphology and size are two crucial parameters of abrasives for CMP applications. Fig. 2, Figs. S2(b)-(f) and Figs. S3(b)-(f) show the SEM images of $\text{Ce}_{1-x}\text{Y}_x\text{O}_2$, $\text{Ce}_{1-x}\text{La}_x\text{O}_2$ and $\text{Ce}_{1-x}\text{Pr}_x\text{O}_2$ abrasives, respectively. It can be seen from Fig. 2 (a) that pure CeO_2 abrasives are spherical particles with an average size of $\sim 238.10 \text{ nm}$. However, this situation is changed by Y^{3+} doping. On the one hand, the size of abrasives is significantly reduced with the increase of doping. On the other hand, the morphology of abrasives changes to octahedron with the incorporation of Y^{3+} . In addition, as shown in Figs. S2(b)-(f) and Figs. S3(b)-(f), the change of $\text{Ce}_{1-x}\text{La}_x\text{O}_2$ and $\text{Ce}_{1-x}\text{Pr}_x\text{O}_2$ abrasives is more significant with doping. Fig. S4 summarizes the average size of the $\text{Ce}_{1-x}\text{M}_x\text{O}_2$ abrasives, which shows that the particle size is affected by the types and amounts of doping. In the same amount, the incorporation of ions with larger radius is more likely to lead to the reduction of particle size. In the same type, the more doping, the smaller the particle size. Fig. S5 shows EDS mapping images of pure and Y^{3+} doped, La^{3+} doped and Pr^{3+} doped CeO_2 abrasives with a doping amount of 0.10. All known elements of the samples were identified and no other irrelevant elements were detected. And the distribution of all elements is consistent with the dispersion of the samples, which also reflects the formation of the Ce-M-O solid solution [30]. In addition, the EDS spectra corresponding to pure CeO_2 , $\text{Ce}_{0.9}\text{La}_{0.1}\text{O}_2$, $\text{Ce}_{0.9}\text{La}_{0.1}\text{O}_2$ and $\text{Ce}_{0.9}\text{La}_{0.1}\text{O}_2$ samples are shown in Fig. 3 (a)-(d). It is observed that the elements in the corresponding spectra of all samples are present in nearly stoichiometric ratio. The atomic ratios of Y, La and Pr atoms in the samples are 2.05, 1.11 and 1.62 at%,

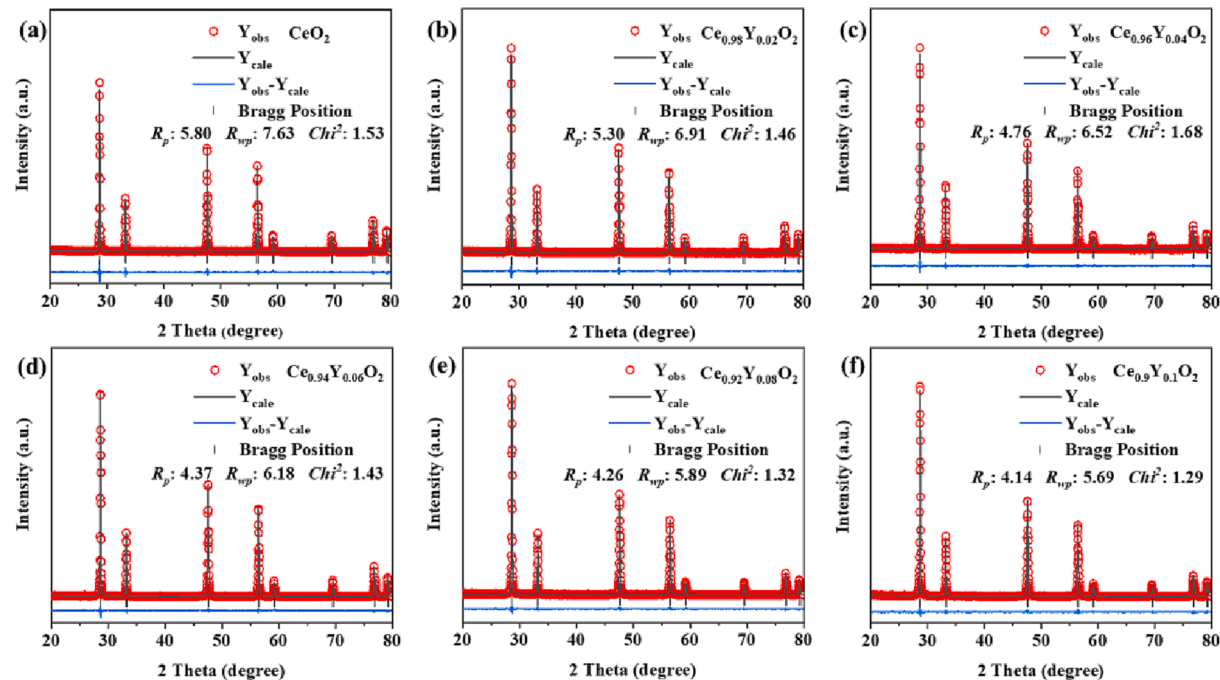


Fig. 1. The Rietveld refinement patterns of $\text{Ce}_{1-x}\text{Y}_x\text{O}_2$ abrasives, (a) $x = 0.02$; (b) $x = 0.04$; (c) $x = 0.06$; (d) $x = 0.08$; (e) $x = 0.10$.

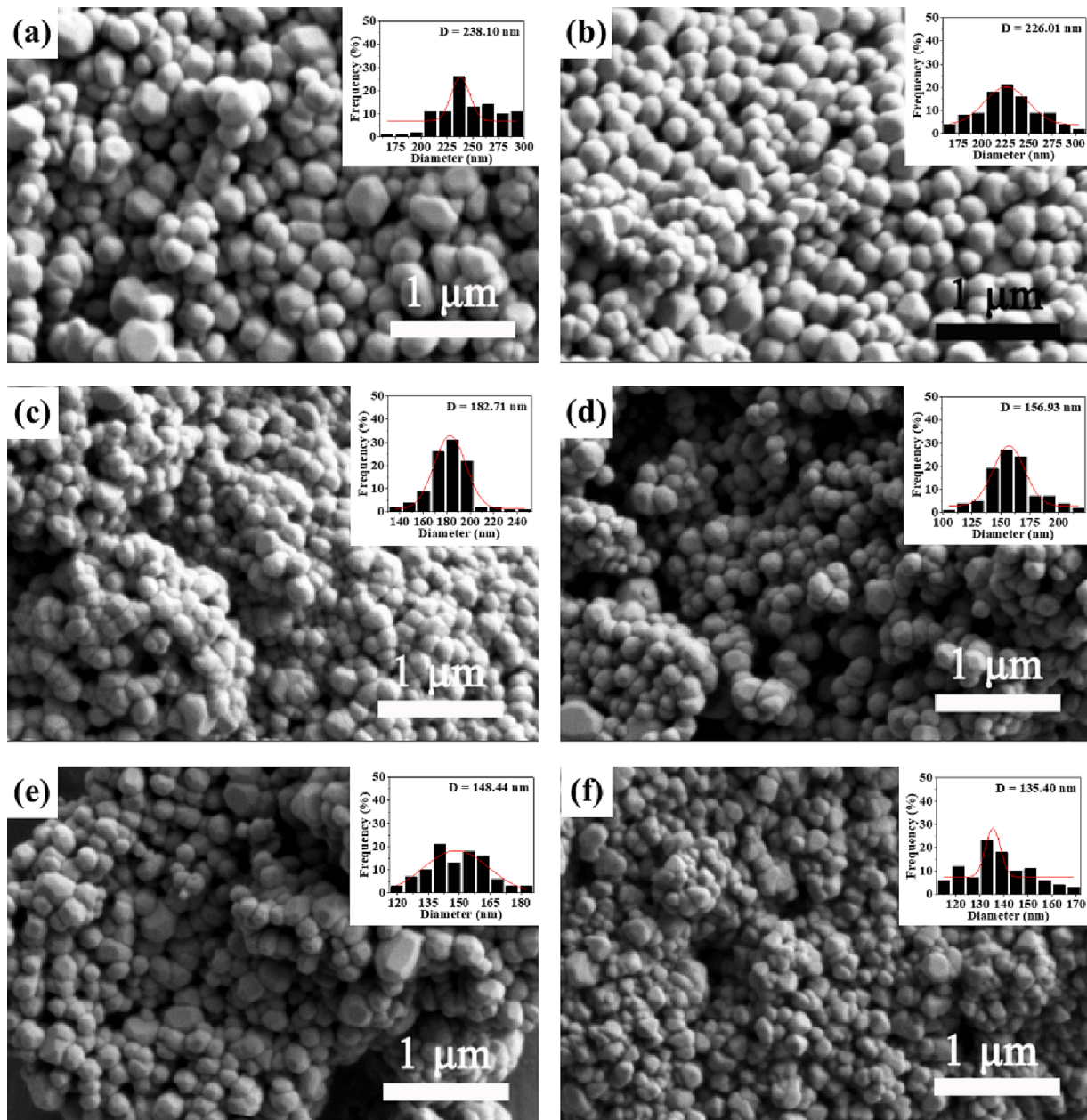


Fig. 2. SEM images and the size distribution of Ce_{1-x}Y_xO₂ abrasives ($x = 0.00, 0.02, 0.04, 0.06, 0.08, 0.10$).

respectively, which also reflects that ions with smaller radii are more likely to be incorporated.

3.3. DFT analysis

The electronic structure of the ideal CeO₂ crystal is calculated in order to analyze the effect of doping on the electronic structure of CeO₂ phase. Fig. S6 (a) shows the calculated spin up electron density of state (DOS) of CeO₂ structure. In this work, the DOS near the Fermi level is analyzed, which mainly reflects the electronic properties of the system. The electron states near the Fermi level are divided into two regions, which are the valence band of -5 ~ 0 eV and the conduction band of 0 ~ 5 eV [31]. The electron states in the valence region are mainly composed of O 2p, Ce 5d and Ce 4f orbitals, which correspond to the highest occupied molecular orbital (HOMO) of CeO₂. The electron states in the conduction region are mainly composed of empty Ce 4f orbitals without electrons, which corresponds to the lowest unoccupied molecular orbital (LUMO) [32]. The calculated band gap width of O 2p state is

about 4.0 eV, and the band gap between O 2p and Ce 4f state is about 2.3 eV, which is consistent with the results in the report [26]. According to the energy band theory of solids, the prerequisite for a good conductor is that the Fermi energy level intersects one or more energy bands and the band is wide. It can be seen from Fig. S6(a) that CeO₂ does not meet the condition, which also indicates that CeO₂ is a weakly conductive material. In addition, the band gap of CeO₂ is large, the covalent bond is strong, and the ionic bond is weak, which is the reason for its weak electrical conductivity. Fig. 3 also pointed out that there are empty f orbitals near the Fermi level of CeO₂, which makes it easy for electrons to be stored in them [17]. This also explains the fundamental reason for the unique performance of CeO₂ materials from a microscopic perspective. Figs. S6(b) shows the XRD patterns of pure and the doped CeO₂ by simulation. The peak of the doped sample shifts to a lower angle, which is consistent with the experimental results.

Fig. 4 shows the DOS of CeO₂ system including dopants and oxygen vacancy. The red curves describe the DOS of the unreduced systems in the Figs. Different from pure CeO₂, it can be seen that a hole state in its O

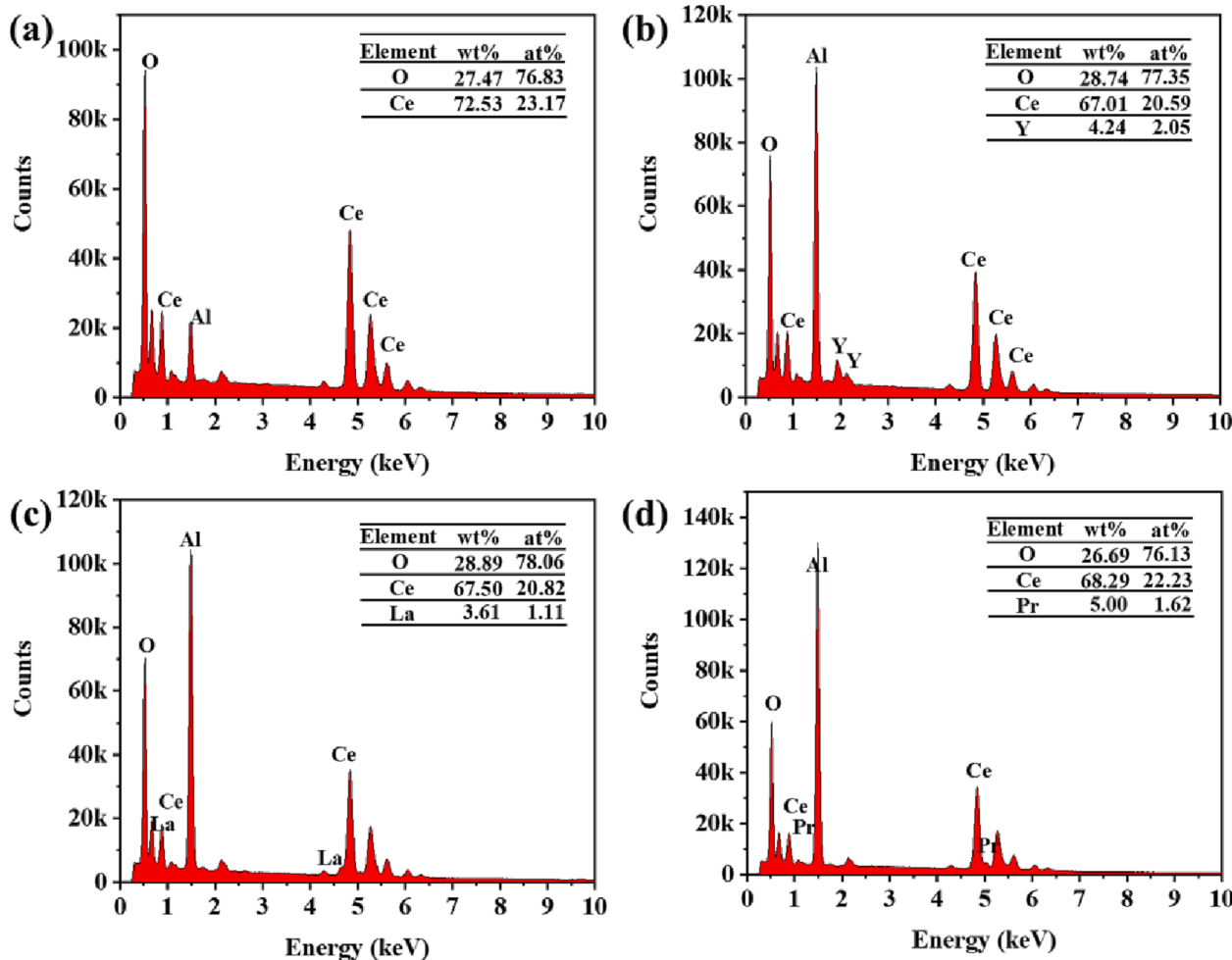


Fig. 3. EDS spectra of the pure CeO₂, Ce_{0.9}Y_{0.1}O₂, Ce_{0.9}La_{0.1}O₂ and Ce_{0.9}Pr_{0.1}O₂ samples.

2p state at the top of the valence band in the doped CeO₂ system, which is attributed to the +4-valent Ce is replaced by the +3-valent impurity. The electrons left by the formation of oxygen vacancies are accepted by the O 2p state, which results in the reduction of oxygen vacancy formation energy. The blue curves represent the DOS of the reduced systems, the DOS of the reduced systems moves towards the lower energy level compared with the unreduced systems, which is caused by the generation of oxygen vacancies. After the system is reduced, a new gap state appears near the Fermi level, which is consistent with other studies [33,34]. The gap state is mainly from the Ce 4f state, which indicates that the Ce 4f orbital is partially occupied by two electron generated after the formation of the oxygen vacancy. And the electron of Ce 4f state is localized on the Ce ion around the oxygen vacancy, which will promote the two neighboring Ce⁴⁺ reduction to Ce³⁺.

The electronic structure of the reduced systems are significantly changed compared with the unreduced systems. Therefore, the vacancy formation energy of doped and undoped CeO₂ systems were studied. The oxygen vacancy formation energies (E_{vac}) are calculated using Eq. (2) [35].

$$E_{\text{vac}} = E_{\text{cell-vac}} + 1/2E(O_2) - E_{\text{cell}} \quad (2)$$

where $E_{\text{cell-vac}}$ and E_{cell} are the total energy of the supercell with and without an oxygen vacancy, respectively, and $E(O_2)$ represents the total energy of the ground state of a free O₂ molecule. The positive E_{vac} values indicate that the formation of the O vacancy requires the provision of additional energy. The calculated energy values are shown in Table 2, the E_{vac} required for the generation of each oxygen vacancy in pure CeO₂

is 3.4985 eV, which is similar to the other results. And the E_{vac} of Y³⁺-CeO₂, La³⁺-CeO₂ and Pr³⁺-CeO₂ are 0.8517, 1.0228 and 1.0028 eV, respectively. The E_{vac} of all doping CeO₂ systems is significantly reduced compared with the pure, which indicate M³⁺ doping is very favorable to the formation of oxygen vacancy. The oxygen vacancy is closely related to the transition from Ce⁴⁺ to Ce³⁺ in CeO₂, and the reduction of the E_{vac} greatly promotes the generation of Ce³⁺ [36].

Furthermore, the repulsion between positive charges in the CeO₂ lattice is reduced by M³⁺ doping, which reduces the energy of the systems. However, the Table 2 shows that the cell energy is increased after the M³⁺ doping. The reason is that the lattice constant is increased caused by doping, which enhances the residual stress generated in the crystallization of CeO₂ phase [17]. Therefore, a large amount of M³⁺ doping is not conducive to the stability of CeO₂ phase.

3.4. XPS analysis

The elemental composition of the actual sample and the corresponding Ce element valence information were characterized by XPS technology. Fig. 5(a) shows the XPS survey spectra of the samples. The peaks of Ce and O elements are calibrated in all the spectra. The specific peaks of Y, La and Pr elements were only identified in Ce_{0.9}Y_{0.1}O₂, Ce_{0.9}La_{0.1}O₂ and Ce_{0.9}Pr_{0.1}O₂ samples, respectively, which also support the EDS results. Fig. 5(b)-(e) show the Ce 3d fine spectra of the samples. The Ce 3d level is composed of two pairs of spin orbital doublet of 3d_{3/2} and 3d_{5/2} [36]. The peaks attributed to the Ce 3d core level is formed by fluctuations in the electronic states of the Ce 4f level, which reflect the changes between Ce³⁺ and Ce⁴⁺. Therefore, the Ce 3d spectra were

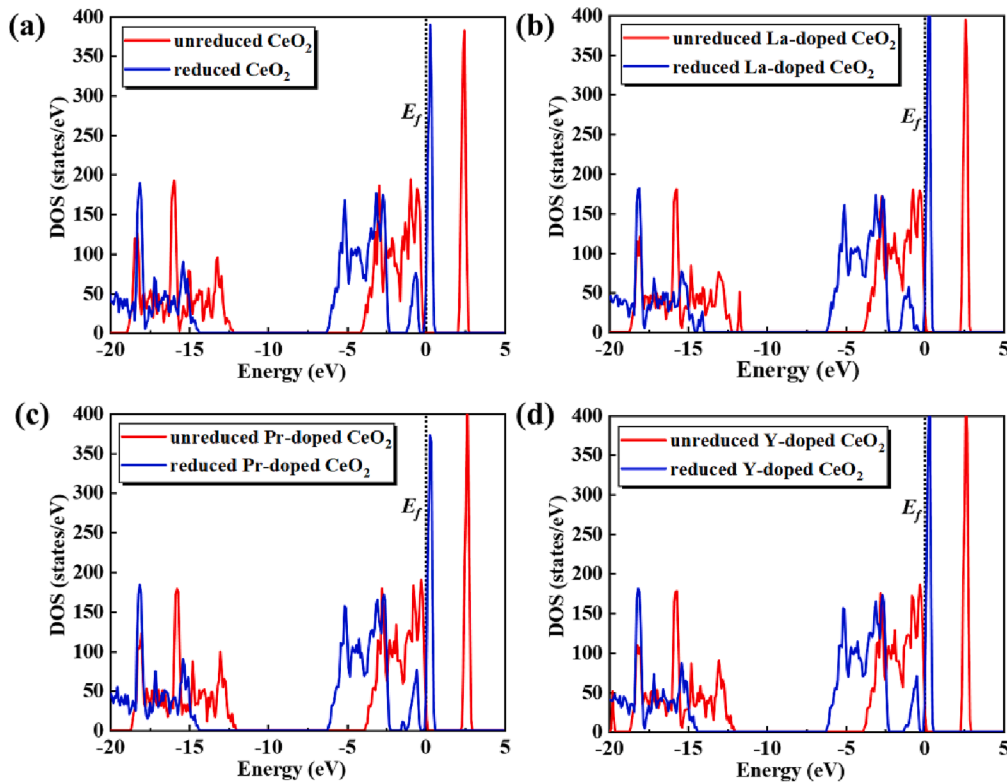


Fig. 4. The density of states (DOS) of CeO_2 including dopants and oxygen vacancy.

Table 2
The energies of CeO_2 systems calculated by DFT.

	CeO_2	$\text{Y}^{3+}\text{-CeO}_2$	$\text{La}^{3+}\text{-CeO}_2$	$\text{Pr}^{3+}\text{-CeO}_2$
$E(\text{O}_2)$	-2.6729			
$E_{\text{cell-vac}}$	-516.9119	-519.5382	-517.6054	-517.1504
E_{cell}	-521.7469	-521.7264	-519.9647	-519.4897
E_{vac}	3.4985	0.8517	1.0228	1.0028

further analyzed by the nonlinear peak fitting method. The peaks of the spin orbits $3d_{3/2}$ and $3d_{5/2}$ are labeled with u and v , respectively. And the peaks labeled v , v' , v'' , u , u' , and u'' belong to the peaks of Ce^{4+} , and the peaks labeled v_0 , v' , u_0 , and u' represent Ce^{3+} [37]. The peaks of Ce^{3+} and Ce^{4+} are identified in all the samples, which indicate that Ce have mixed valence states of + 3 and + 4 in the samples. The binding energy and area of the corresponding peaks are collected in Table 3. The valence state of Ce is semi-quantitatively analyzed by using the area

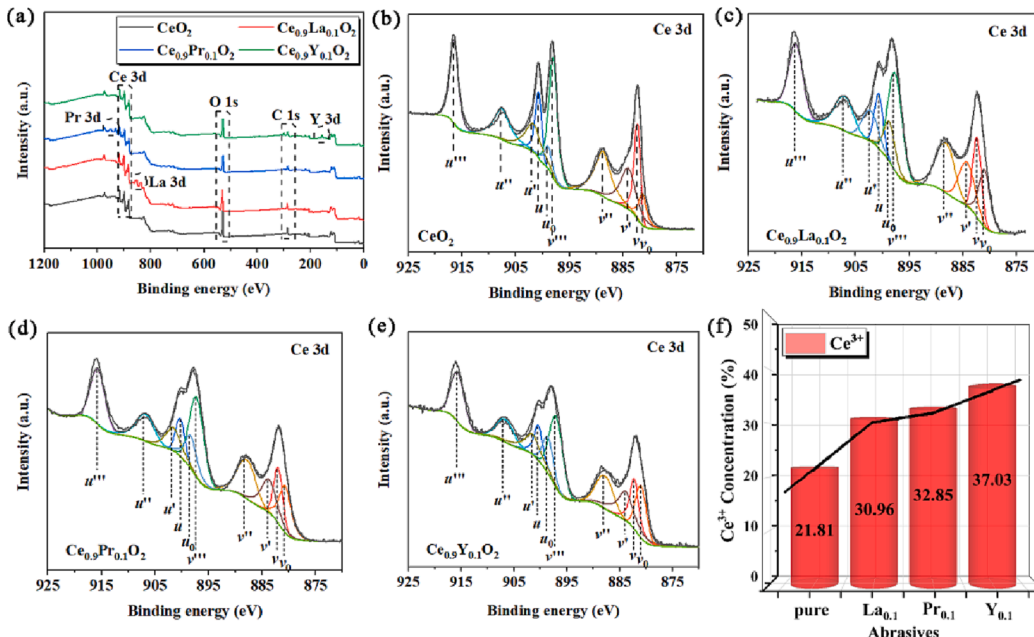


Fig. 5. XPS spectra of CeO_2 abrasives: (a) Survey; (b)-(e) Ce 3d spectra of CeO_2 , $\text{Ce}_{0.9}\text{La}_{0.1}\text{O}_2$, $\text{Ce}_{0.9}\text{Pr}_{0.1}\text{O}_2$ and $\text{Ce}_{0.9}\text{Y}_{0.1}\text{O}_2$, respectively; (f) Ce^{3+} concentration of the abrasive surfaces.

Table 3

Binding energies and peak areas representing different Ce states in the $\text{Ce}_{1-x}\text{M}_x\text{O}_2$ samples.

Pure CeO_2	v_0	v	v'	v''	v'''	u_0	u	u'	u''	u'''
BE(eV)	881.33	882.22	883.99	888.72	898.00	898.93	900.64	901.71	907.54	916.47
Area(%)	5.67	16.91	7.26	7.99	21.27	3.92	11.71	4.99	5.54	14.75
$\text{Ce}_{0.9}\text{Y}_{0.1}\text{O}_2$										
BE(eV)	880.97	882.19	883.89	887.66	897.04	898.57	900.34	901.49	906.56	915.67
Area(%)	10.22	9.39	11.60	10.46	17.36	7.08	6.50	8.13	7.24	12.02
$\text{Ce}_{0.9}\text{La}_{0.1}\text{O}_2$										
BE(eV)	880.95	882.36	884.42	888.02	897.64	898.55	900.68	902.44	906.92	916.07
Area(%)	9.03	9.14	9.26	13.57	18.26	6.25	6.33	6.41	9.10	12.64
$\text{Ce}_{0.9}\text{Pr}_{0.1}\text{O}_2$										
BE(eV)	880.66	882.00	883.74	887.68	897.21	898.26	900.27	901.56	906.58	915.66
Area(%)	10.28	8.39	9.13	12.78	18.66	7.12	5.76	6.32	8.63	12.92

ratio of the peaks according to the Eq. (3) [36].

$$\frac{\text{Ce}^{3+}}{\text{Ce}^{3+} + \text{Ce}^{4+}} = \frac{\text{area}(v_0, u_0, v', u')}{\text{totalarea}} \quad (3)$$

Fig. 5(f) shows the Ce^{3+} concentration of the abrasive surfaces. The Ce^{3+} concentration of the pure CeO_2 abrasives is 21.81 %, and the Ce^{3+} concentration is significantly improved by doping. Specifically, the Ce^{3+} concentration on the surface of $\text{Ce}_{0.9}\text{Y}_{0.1}\text{O}_2$, $\text{Ce}_{0.9}\text{La}_{0.1}\text{O}_2$ and $\text{Ce}_{0.9}\text{Pr}_{0.1}\text{O}_2$ abrasives are 37.03, 30.96 and 32.85 %, respectively. The results are consistent with the E_{vac} calculated by DFT. The oxygen vacancy formation energy in CeO_2 crystals is reduced by doping, which significantly promotes the transition from Ce^{4+} to Ce^{3+} . The abundant Ce^{3+} in CeO_2 abrasives is crucial for the improvement of CMP performance [8]. The mechanism of Ce valence transition induced by M^{3+} doping is analyzed in the next section.

3.5. Formation mechanism of Ce^{3+} induced by ion doping

The free electrons generated in the CeO_2 system are easily stored due to the presence of Ce 4f orbitals [17], which is also the reason for the

transition of Ce^{4+} to Ce^{3+} . As previously calculated by the DFT, the generation of intrinsic oxygen vacancies is difficult due to the high energy required, which greatly restricts the transition of Ce valence. The CeO_2 system can obtain the benefit of high oxygen vacancy concentration at the cost of only low impurity introduction by doping. Fig. 6 shows the schematic diagram of the structural evolution of CeO_2 crystal after doping. The trivalent M^{3+} is incorporated into the CeO_2 lattice, which replaces the high valence Ce^{4+} . In order to maintain the charge balance inside the lattice, the lattice oxygen is diffused to the outside in the way of Eq. (4), while oxygen vacancies are generated in the lattice, as shown in Eq. (5). In addition, the overflow of molecular oxygen releases two free electrons in its vacancy to maintain electrical neutrality, as shown as Eq. (6) and Fig. 6(a). Meanwhile, the positive ions around the oxygen vacancy obtain the electrons, which results in the reduction of the Ce valence, as shown in Eq. (7) [18]. It's worth noting that the electrons don't permanently bind to a certain Ce^{4+} to bring its valence down to +3. That is, the electron doesn't belong to a certain Ce^{4+} , but moves around the vacancy under the control of the electric field, which makes it easy for the electron to migrate from one Ce^{4+} site to another. Fig. 6(b) shows the ideal evolution behavior. At a certain moment, an electron

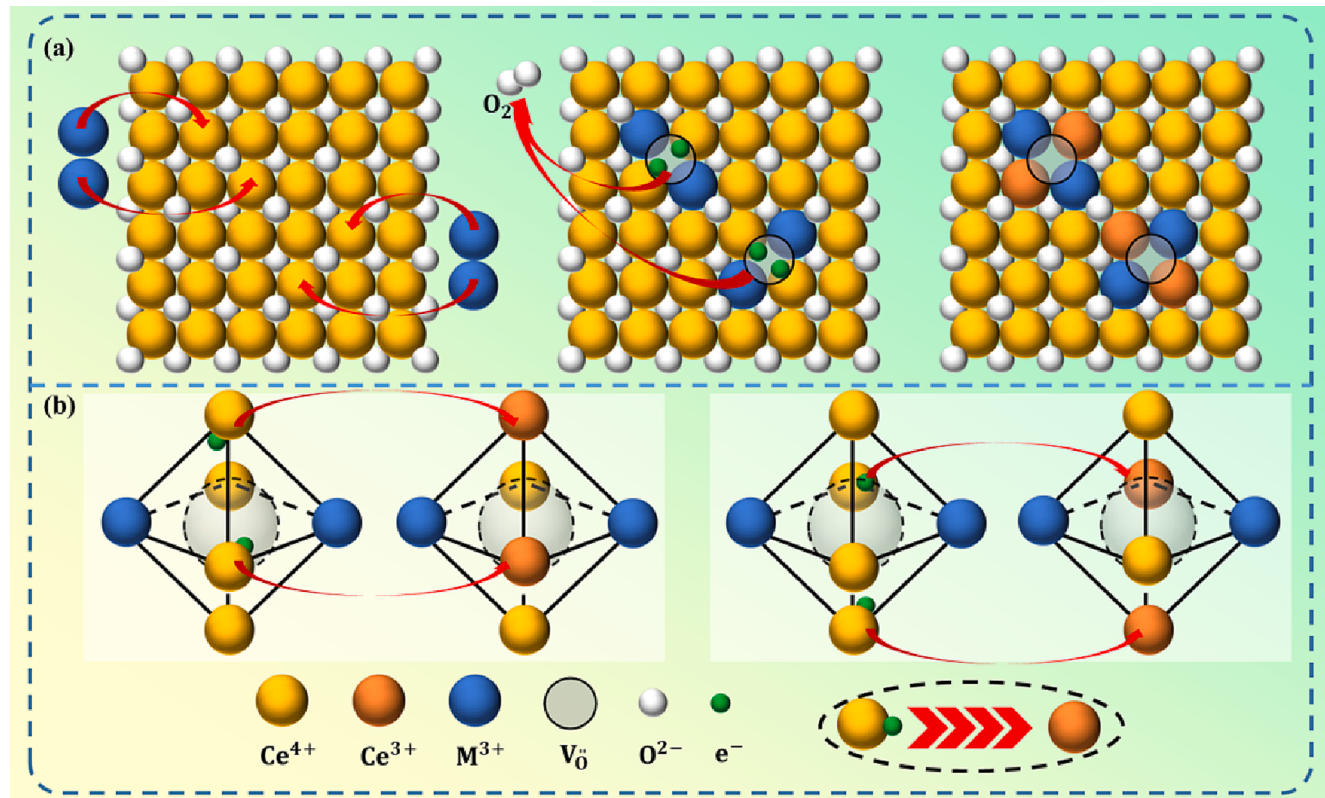
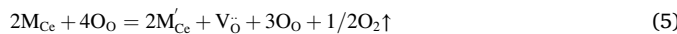
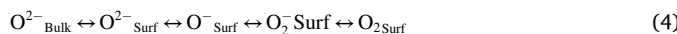


Fig. 6. Schematic diagram of the structural evolution of CeO_2 crystal doped with M^{3+} .

attaches to a nearby Ce^{4+} , which temporarily gains this electron and becomes Ce^{3+} , and at another moment, this electron combines with another Ce^{4+} .



3.6. Material removal rate (MRR)

The relentless pursuit of the MRR not only optimizes manufacturing time, but also saves the cost of the slurry. Fig. 7 shows the MRR of SiO_2 substrates polished with the slurries containing pure, Y^{3+} doped, La^{3+} doped and Pr^{3+} doped abrasives. The MRR of pure CeO_2 abrasives is 401.90 nm. The MRRs of $\text{Ce}_{1-x}\text{Y}_x\text{O}_2$ abrasives with different amounts of Y^{3+} doping are 509.10, 578.74, 589.46, 626.97 and 562.67 nm/min, respectively. This illustrates that the polishing efficiency of all the abrasives are improved by Y^{3+} doping. The detailed analysis shows that the $\text{Ce}_{0.92}\text{Y}_{0.08}\text{O}_2$ abrasives has the highest MRR in a series of $\text{Ce}_{1-x}\text{Y}_x\text{O}_2$ abrasives, and its MRR increased by 56 % compared with that of the pure. In addition, the CMP performance of $\text{Ce}_{1-x}\text{La}_x\text{O}_2$ and $\text{Ce}_{1-x}\text{Pr}_x\text{O}_2$ abrasives were also tested synchronously. The trend of MRR of La^{3+} doped and Pr^{3+} doped abrasives are improved with the amount of doping are increased, which is consistent with Y^{3+} doped abrasives. For a certain doping amount, there is no significant difference in the morphology of all kinds of abrasives, and the enhancement of MRR is mainly attributed to the elevation of Ce^{3+} concentration. At a low doping levels, even if the abrasive has a large particle size, it cannot achieve a high MRR due to its low chemical activity. That is, the chemical activity of the abrasive is the dominant factor affecting its MRR at low doping. Whereas, at high doping levels, the smaller particle size achieves a higher removal performance due to the higher chemical activity. For a certain doping type, the morphology of the abrasive changes from spherical to octahedral, the particle size gradually decreases, and the concentration of Ce^{3+} on the abrasive surface increases with the doping amount increases. A number of factors combine to cause changes in the MRR of abrasives. The continuous reduction of particle size is not conducive to the improvement of MRR. Therefore, the morphological transition and the improvement of Ce^{3+} concentration caused by the

continuous increase of doping amount are the key to promote MRR. However, the morphology of the abrasive tends to stabilize after $x = 0.04$, and its enhancement of the MRR is not significant at higher doping levels. The comprehensive analysis of the above results shows that the polishing efficiency of abrasives is improved by M^{3+} doping, which is obviously attributed to the increase of Ce^{3+} concentration. It is worth noting that the $\text{Ce}_{0.92}\text{Y}_{0.08}\text{O}_2$ abrasives show an excellent removal performance, which is contributed to the synergistic effect of the chemical and mechanical of the abrasives on the substrate is relatively optimal when the doping amount (x) is 0.08. Similarly, $\text{Ce}_{0.92}\text{La}_{0.08}\text{O}_2$ and $\text{Ce}_{0.92}\text{Pr}_{0.08}\text{O}_2$ abrasives obtain MRRs of 562.66 and 578.74 nm/min, respectively, which corresponds to the best performance in their groups. However, the mechanical action of the abrasives is significantly reduced due to the small particle size when the doping amount continues to increase, and the imbalance of the synergy leads to the decrease of its MRR. In addition, the relatively small abrasives is more likely to be embedded in the polishing pad with a groove structure, which makes them to be invalid in polishing. This result also reflects the fact that a certain particle size is necessary for the abrasives.

3.7. Surface quality

The high precision and low damage to the polished surface are the advantages of CMP over other flattening techniques [27]. Therefore, the surface quality of the polished surface of the substrates were characterized by AFM. The 2-dimensional (2D) height images and the corresponding line roughness curves of the quartz glass surface before and after polishing were obtained. In the 2D-AFM images, the dark and light areas present valley and crest of the surface, respectively, which means that the lower the contrast ratio of the color, the better the surface quality of the material. Meanwhile, the low peak-to-peak (pk-pk) also reflects the excellent surface smoothness from the line profile curves. Fig. 8(a)-(c) are the evaluated surface quality of the initial quartz glass. Many pits and scratches were observed on the surface, which indicates its poor condition. The line profile with a pk-pk value of 6.08 nm and the uneven 3D surface also indicate bad conditions. As shown in Fig. 8(d)-(f), a significantly improved surface (the surface is nearly smooth, and the pk-pk value of the line profile is only 1.37 nm) was observed after polishing with the pure CeO_2 abrasives, which reflects the key role of CeO_2 abrasives in CMP. Fig. 9 shows AFM images and corresponding line profile curves of SiO_2 substrates after CMP with $\text{Ce}_{1-x}\text{Y}_x\text{O}_2$ abrasives. The surface quality of the polished glass is significantly improved compared with the initial quartz glass, and the pk-pk of the line profile curves of all samples reach ~ 1.00 nm. The AFM evaluation after polishing using $\text{Ce}_{1-x}\text{La}_x\text{O}_2$ and $\text{Ce}_{1-x}\text{Pr}_x\text{O}_2$ abrasives are shown in Figs. S8 and S9, respectively, and they all show excellent results. Fig. 10 shows the average roughness (R_a) of the surface of quartz glass. For all kinds of the abrasives, the surface roughness of the quartz glass was reduced from ~ 2.3 nm to below 0.8 nm after polishing. Particularly, all kinds of doped abrasives show the best polishing quality for quartz glass when the doping amount is 0.04, which may be due to the relative balance of the action between the chemical and mechanical of the abrasives in the CMP. Furthermore, the performance of Y^{3+} doped CeO_2 abrasives is better than that of La^{3+} doped and Pr^{3+} doped abrasives at the same doping amount.

3.8. CMP mechanism

Fig. 11 presents the schematic diagram of CMP mechanism for CeO_2 abrasives to SiO_2 substrate. In the CMP system, the polishing pad and slurry are in direct contact with the SiO_2 substrate [38]. The dispersed abrasives act as the carrier for the synergy of chemical and mechanical in CMP, and the study of its removal mechanism is worth thinking about. Therefore, based on the intuitive experimental data in this work, the role of CeO_2 abrasives in direct contact with SiO_2 substrate was mainly analyzed. The doped CeO_2 abrasives shows a continuous reduction in

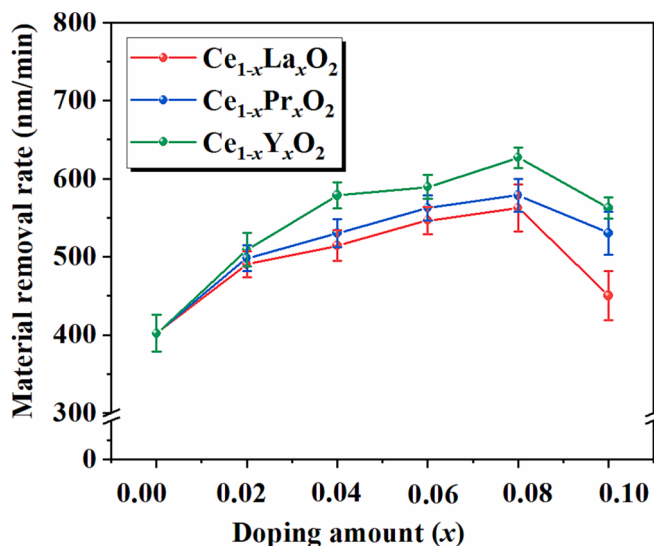


Fig. 7. Material removal rates of $\text{Ce}_{1-x}\text{Y}_x\text{O}_2$, $\text{Ce}_{1-x}\text{La}_x\text{O}_2$ and $\text{Ce}_{1-x}\text{Pr}_x\text{O}_2$ abrasives ($x = 0.00, 0.02, 0.04, 0.06, 0.08, 0.10$) on quartz glass substrates.

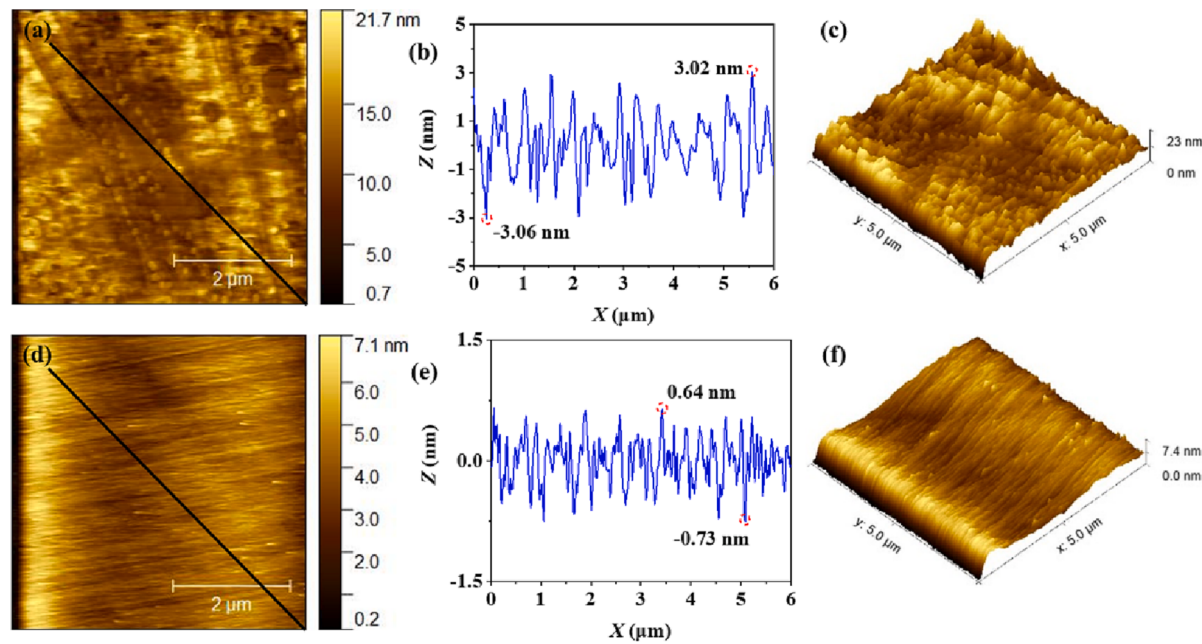


Fig. 8. AFM images and corresponding line profile curves of SiO₂ substrates: (a)-(b) Initial surface before CMP; (c)-(d) Surface after CMP with CeO₂ abrasives.

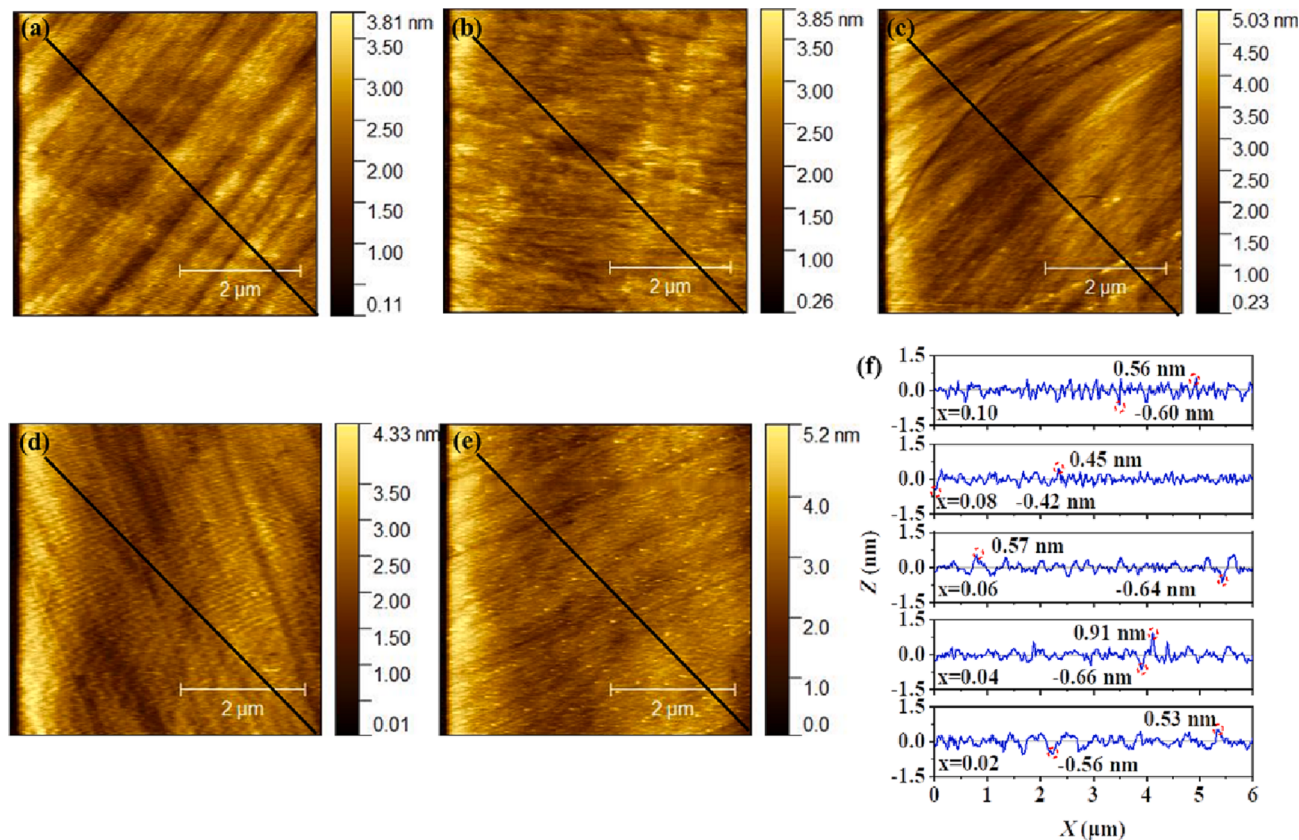


Fig. 9. AFM images and corresponding line roughness curves of SiO₂ substrates after CMP with Ce_{1-x}Y_xO₂ abrasives: (a) $x = 0.02$; (b) $x = 0.04$; (c) $x = 0.06$; (d) $x = 0.08$; (e) $x = 0.10$ and (f) Line profile curves.

size, which affects the CMP performance to a certain extent. As shown in Fig. 11(a), the small size abrasives exhibit a considerable amount compared to the large abrasives at the same solid content. However, some of the abrasives are stored in the grooves and become invalid particles because the pad usually has a special groove structure [39].

The proportion of valid abrasives in direct contact with the surface increases with the size, which means the improvement of MRR. In addition, the contact stress at the abrasives-substrate interface is shared by the large amount of abrasives, which makes the removal depth of the abrasives to the substrate shallower. In contrast, the large abrasives have

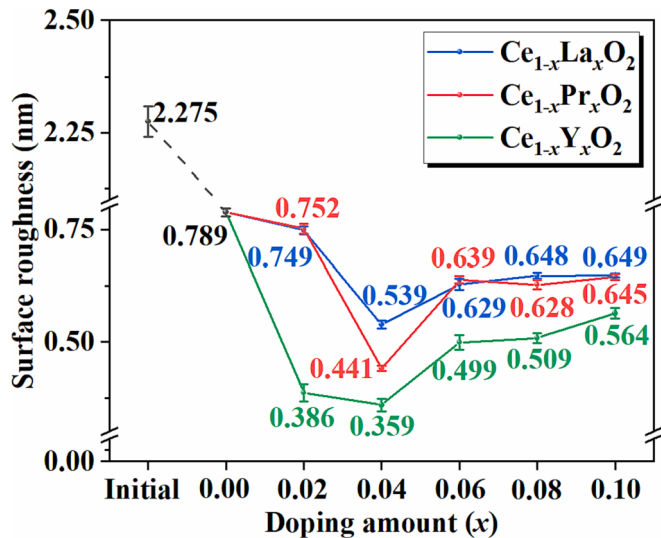


Fig. 10. The results of evaluation for surface roughness of SiO_2 substrates after CMP using $\text{Ce}_{1-x}\text{Y}_x\text{O}_2$, $\text{Ce}_{1-x}\text{La}_x\text{O}_2$ and $\text{Ce}_{1-x}\text{Pr}_x\text{O}_2$ abrasives ($x = 0.00, 0.02, 0.04, 0.06, 0.08, 0.10$).

a strong local load on the substrate, which usually corresponds to a relatively low polishing quality [40]. Therefore, the medium sized abrasives that have a balance between polishing efficiency and quality is a good choice.

As far as the macroscopic changes of the abrasives is concerned, the doped abrasives also show a morphological transition from spherical to octahedral. As shown in Fig. 11(b), the octahedral abrasives has larger removal depth due to larger local force under the same load, which results in enhanced polishing efficiency [41]. In CMP, the motion modes of abrasives include sliding and rolling. The spherical abrasives are more likely to show rolling behavior, which also makes abrasives exhibit adhesive wear in the material removal. The study of Hoshino et al. [42] showed that the surface of the abrasives was attached with SiO_2 lumps after polishing, which confirmed this view. The octahedral particles with sharp edges show sliding friction, which significantly enhances MRR due to the groove wear. Furthermore, the local heat is generated due to continuous mutual friction at the interface, which makes the chemical reaction between CeO_2 abrasives and SiO_2 substrate more intense [43]. Similarly, the influence of the change of morphology on the polishing efficiency and quality is contradictory.

The advantage of CeO_2 abrasives over the others is its unique chemical activity, which makes it to achieve high removal efficiency at low solid content [20,38]. The perfect CeO_2 crystals lacking Ce^{3+} exhibit poor performance in a variety of applications including CMP [19,44,45].

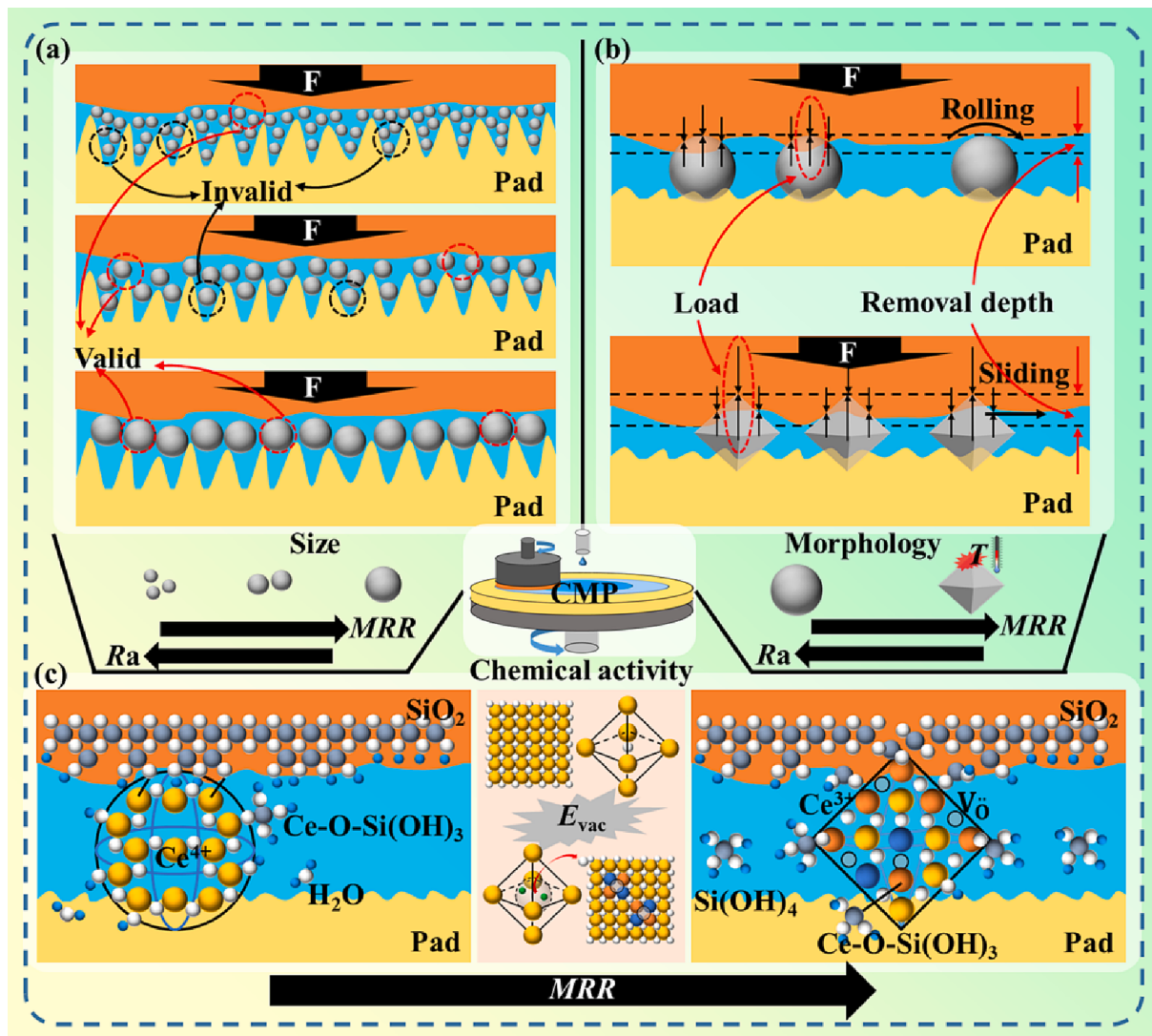


Fig. 11. Schematic diagram of the CMP mechanism for CeO_2 abrasives on SiO_2 substrate.

Fig. 11(c) shows the polishing behavior of CeO₂ abrasives. The polishing behavior of pure CeO₂ abrasives follows the chemical tooth theory proposed by Cook [46]. In the slurry, the surface of the SiO₂ substrate is hydrolyzed into hydrogen-terminated -Si-OH species (“soft layer”), and the chemical reaction between the abrasive and the layer forms a Ce-O-Si bond. It is worth noting that the Ce-O bond is a covalent bond with stronger polarity, while the Si-O bond has a lower bond strength due to the stronger bond length. This means that the Si-O bonds are more easily broken under the traction of mechanical force to achieve the removal. In recent years, the enhancement of CMP performance by Ce³⁺ concentration on CeO₂ abrasive surface has attracted more and more attention. As discussed above, the E_{vac} of CeO₂ crystal is significantly reduced after doping, and the free electrons trapped in the vacancy promote the transition of Ce⁴⁺ to Ce³⁺. Ce³⁺ as the active species promoted the removal, which was also confirmed by the CMP experiments. Seo et al. [47] showed that Ce³⁺ has stronger adsorption behavior for silicate than Ce⁴⁺ through theoretical calculation, which was also confirmed by experiments conducted by Myong et al. [48]. It can be seen that the increase of Ce³⁺ concentration on the surface of CeO₂ abrasives greatly improves the contact probability between the abrasives and SiO₂ substrate, which promotes the chemical bonding at the interface. Directly, the transition from Ce⁴⁺ to Ce³⁺ acts as a “reservoir” for electrons. After the Ce-O-Si bond is formed, the stored electrons are transferred to the Si-O bond through the linked bond, which further weakens or breaks the Si-O bond. The bond breaking caused by chemical action significantly improves the efficiency of the breaking only by mechanical action.

Furthermore, CMP is still a dynamic process that combines multiple physical scales. The final CMP performance is determined by the combination of multiple physical parameters. It is a proper research method to reveal the CMP mechanism by means of multi-physical field coupling technique and finite element analysis. That's what we're going to do next.

4. Conclusion

In this work, we prepared a series of CeO₂ abrasives with different types and amounts of doping by molten salt method for improving the CMP performance. SEM images show that all abrasives have uniform size and morphology. For all types of the doped abrasives, the morphology of abrasives changes from spherical to octahedral and the particle size also decreases with the doping increases. The larger the radius of the doped ions is, the more obvious the size change of the doped abrasives is. These visual changes in abrasives have significant influence on the CMP performance. The DOS and E_{vac} of pure, Y³⁺-doped, La³⁺-doped, and Pr³⁺-doped CeO₂ abrasives were calculated using DFT. The E_{vac} of CeO₂ crystal is significantly decreased by doping. In particular, Y³⁺-doped abrasives have the lowest E_{vac} than La³⁺ and Pr³⁺-doped abrasives, which means that it is more favorable for the transition from Ce⁴⁺ to Ce³⁺. It was also confirmed by XPS that the Ce³⁺ concentration on the doped CeO₂ abrasive surface was significantly improved. CMP experiments show that the polishing efficiency of abrasives is enhanced by doping, but it does not improve linearly with the increase of doping. It is affected by the size, morphology and defects of the abrasives. The increased Ce³⁺ concentration and octahedral morphology of abrasives are responsible for the enhanced the polishing efficiency, which is regulated by doping. However, the size of the abrasives decreases with the doping continues to increase, which makes the MRR of the abrasives present a net decrease at larger doping levels. Therefore, the selection of appropriate type and amount of doping is the key point to improve the CMP performance. This study is expected to provide a scientific and reasonable method for the selection of the type and amount of doping for the preparation of doped abrasives. The molten salt method used is also a potential method for preparing CeO₂ particles. In addition, the polishing mechanism of CeO₂ abrasives on SiO₂ substrate is explained from three perspectives, which will also inspire and promote the theoretical improvement and technological

innovation of CMP.

CRediT authorship contribution statement

Jiahui Ma: Formal analysis, Investigation, Data curation, Software. **Ning Xu:** Funding acquisition, Project administration, Methodology, Resources. **Jinrong Hu:** Formal analysis, Software. **Yuxin Luo:** Software. **Yu Lin:** Writing – review & editing. **Yongping Pu:** Methodology, Supervision.

Declaration of Competing Interest

The authors declare that they have no known competing financial interests or personal relationships that could have appeared to influence the work reported in this paper.

Data availability

No data was used for the research described in the article.

Acknowledgements

This work was financially supported by the National Natural Science Foundation of China (No. 51905324), the Open Foundation of Key Laboratory of Auxiliary Chemistry and Technology for Chemical Industry (No. KFKT2022-09), the Shaanxi Collaborative Innovation Center of Industrial Auxiliary Chemistry and Technology of Shaanxi University of Science and Technology (No. KFKT2022-09), and the China Postdoctoral Science Foundation (No. 2022MD713771).

Appendix A. Supplementary material

Supplementary data to this article can be found online at <https://doi.org/10.1016/j.apsusc.2023.156997>.

References

- [1] Q. Zhang, J. Pan, X. Zhang, J. Lu, Q. Yan, Tribological behavior of 6H-SiC wafers in different chemical mechanical polishing slurries, Wear 472–473 (2021), <https://doi.org/10.1016/j.wear.2021.203649>.
- [2] L. Xie, J. Cheng, T. Wang, X. Lu, Mechanical wear behavior between CeO₂(100), CeO₂(110), CeO₂(111), and silicon studied through atomic force microscopy, Tribol. Int. 153 (2021), 106616, <https://doi.org/10.1016/j.triboint.2020.106616>.
- [3] C. Xiao, F.-C. Hsia, A. Sutton-Cook, B. Weber, S. Franklin, Polishing of polycrystalline diamond using synergies between chemical and mechanical inputs: A review of mechanisms and processes, Carbon 196 (2022) 29–48, <https://doi.org/10.1016/j.carbon.2022.04.028>.
- [4] K. Kawaguchi, Y. Wang, J. Xu, Y. Ootani, Y. Higuchi, N. Ozawa, M. Kubo, Atom-by-Atom and Sheet-by-Sheet Chemical Mechanical Polishing of Diamond Assisted by OH Radicals: A Tight-Binding Quantum Chemical Molecular Dynamics Simulation Study, ACS Appl. Mater. Interfaces 13 (2021) 41231–41237, <https://doi.org/10.1021/acsmami.1c09468>.
- [5] Y. Fan, J. Jiao, L. Zhao, J. Tang, Preparation of lanthanide-doped polystyrene/CeO₂ abrasives and investigation of slurry stability and photochemical mechanical polishing performance, Colloids Surf., A 656 (2023), <https://doi.org/10.1016/j.colsurfa.2022.130508>.
- [6] J. Seo, A review on chemical and mechanical phenomena at the wafer interface during chemical mechanical planarization, J. Mater. Res. (2020) 1–23, <https://doi.org/10.1557/jmr.2020.215>.
- [7] T. Wang, Y. Chen, A. Chen, Y. Chen, Development of carbon sphere/ceria (CS/CeO₂) heterostructured particles and their applications to functional abrasives toward photochemical mechanical polishing, Appl. Surf. Sci. 593 (2022), 153449, <https://doi.org/10.1016/j.apsusc.2022.153449>.
- [8] R. Srinivasan, P.V.R. Dandu, S.V. Babu, Shallow Trench Isolation Chemical Mechanical Planarization: A Review, ECS J. Solid State Sci. Technol. 4 (2015) P5029–P5039, <https://doi.org/10.1149/2.0071511jss>.
- [9] Y.H. Kim, Y.G. Jung, G.S. Yoon, J. Moon, A. Watanabe, M. Naito, U. Paik, Non-Prestonian behavior of rectangular shaped ceria slurry in shallow trench isolation chemical mechanical planarization, J. Nanosci. Nanotechnol. 12 (2012) 2810–2814, <https://doi.org/10.1166/jnn.2012.5780>.
- [10] J.C. Yang, D.W. Oh, G.W. Lee, C.L. Song, T. Kim, Step height removal mechanism of chemical mechanical planarization (CMP) for sub-nano-surface finish, Wear 268 (2010) 505–510, <https://doi.org/10.1016/j.wear.2009.09.008>.

- [11] Y. Chen, R. Long, Polishing behavior of PS/CeO₂ hybrid microspheres with controlled shell thickness on silicon dioxide CMP, *Appl. Surf. Sci.* 257 (2011) 8679–8685, <https://doi.org/10.1016/j.apsusc.2011.05.047>.
- [12] Y. Chen, Z. Li, N. Miao, Polymethylmethacrylate (PMMA)/CeO₂ hybrid particles for enhanced chemical mechanical polishing performance, *Tribol. Int.* 82 (2015) 211–217, <https://doi.org/10.1016/j.triboint.2014.10.013>.
- [13] Y. Chen, Z. Mu, W. Wang, A. Chen, Development of mesoporous SiO₂/CeO₂ core/shell nanoparticles with tunable structures for non-damage and efficient polishing, *Ceram. Int.* 46 (2020) 4670–4678, <https://doi.org/10.1016/j.ceramint.2019.10.198>.
- [14] L. Peedikakkandy, L. Kalita, P. Kavle, A. Kadam, V. Gujar, M. Arcot, P. Bhargava, Preparation of spherical ceria coated silica nanoparticle abrasives for CMP application, *Appl. Surf. Sci.* 357 (2015) 1306–1312, <https://doi.org/10.1016/j.apsusc.2015.09.149>.
- [15] R. Sabia, H.J. Stevens, Performance Characterization of Cerium Oxide Abrasives for Chemical-Mechanical Polishing of Glass, *Mach. Sci. Technol.* 4 (2000) 235–251, <https://doi.org/10.1080/10940340008945708>.
- [16] J. Seo, A. Gowda, S.V. Babu, Almost Complete Removal of Ceria Particles Down to 10 nm Size from Silicon Dioxide Surfaces, *ECS J. Solid State Sci. Technol.* 7 (2018) P243–P252, <https://doi.org/10.1149/2.0131805jss>.
- [17] R. Schmitt, A. Nenning, O. Krainys, R. Korobko, A.I. Frenkel, I. Lubomirsky, S. M. Haile, J.L.M. Rupp, A review of defect structure and chemistry in ceria and its solid solutions, *Chem. Soc. Rev.* 49 (2020) 554–592, <https://doi.org/10.1039/c9cs00588a>.
- [18] J. Paier, C. Penschke, J. Sauer, Oxygen defects and surface chemistry of ceria: quantum chemical studies compared to experiment, *Chem. Rev.* 113 (2013) 3949–3985, <https://doi.org/10.1021/cr3004949>.
- [19] J. Cheng, S. Huang, Y. Li, T. Wang, L. Xie, X. Lu, RE (La, Nd and Yb) doped CeO₂ abrasive particles for chemical mechanical polishing of dielectric materials: Experimental and computational analysis, *Appl. Surf. Sci.* 506 (2020), 144668, <https://doi.org/10.1016/j.apsusc.2019.144668>.
- [20] E. Kim, J. Lee, C. Bae, H. Seok, H.-U. Kim, T. Kim, Effects of trivalent lanthanide (La and Nd) doped ceria abrasives on chemical mechanical polishing, *Powder Technol.* 397 (2022) 117025–117032, <https://doi.org/10.1016/j.powtec.2021.11.069>.
- [21] J. Ma, N. Xu, Y. Luo, Q. Liu, Y. Pu, Defect generation and morphology transformation mechanism of CeO₂ particles prepared by molten salt method, *Ceram. Int.* 49 (2023) 4929–4943, <https://doi.org/10.1016/j.ceramint.2022.10.007>.
- [22] J.P. Perdew, K. Burke, M. Ernzerhof, Generalized Gradient Approximation Made Simple, *Phys. Rev. Lett.* 77 (1997) 3865–11996, <https://doi.org/10.1103/PhysRevLett.77.3865>.
- [23] G. Kresse, J. Furthmüller, Efficient iterative schemes for ab initio total-energy calculations using a plane-wave basis set, *Phys. Rev. B* 54 (16) (1996) 11169–11186, <https://doi.org/10.1103/PhysRevB.54.11169>.
- [24] G. Kresse, J. Furthmüller, Efficiency of ab-initio total energy calculations for metals and semiconductors using a plane-wave basis set, *Comput. Mater. Sci.* 6 (1) (1996) 15–50, [https://doi.org/10.1016/0927-0256\(96\)00008-0](https://doi.org/10.1016/0927-0256(96)00008-0).
- [25] G. Kresse, D. Joubert, From ultrasoft pseudopotentials to the projector augmented-wave method, *Phys. Rev. B* 59 (3) (1999) 1758–1775, <https://doi.org/10.1103/PhysRevB.59.1758>.
- [26] G.E. Murgida, V. Ferrari, M.V. Ganduglia-Pirovano, A.M. Llois, Ordering of oxygen vacancies and excess charge localization in bulk ceria: A DFT+U study, *Phys. Rev. B* 90 (2014), <https://doi.org/10.1103/PhysRevB.90.115120>.
- [27] A. Chen, Y. Duan, Z. Mu, W. Cai, Y. Chen, Meso-silica/Erbium-doped ceria binary particles as functionalized abrasives for photochemical mechanical polishing (PCMP), *Appl. Surf. Sci.* 550 (2021), 149353, <https://doi.org/10.1016/j.apsusc.2021.149353>.
- [28] S. Dai, J. Fu, H. Lei, Y. Chen, Study on the interaction between SiO₂ and ZrO₂ in the chemical mechanical polishing of zirconia ceramic with colloidal silica, *Ceram. Int.* (2021), <https://doi.org/10.1016/j.ceramint.2021.04.177>.
- [29] Z. Sun, X. Wu, D. Guan, X. Chen, J. Dai, Y. Gu, S. She, W. Zhou, Z. Shao, One Pot-Synthesized Ag/Ag-Doped CeO₂ Nanocomposite with Rich and Stable 3D Interfaces and Ce(3+) for Efficient Carbon Dioxide Electroreduction, *ACS Appl. Mater. Interfaces* 13 (2021) 59993–60001, <https://doi.org/10.1021/acsami.1c19529>.
- [30] S. Soni, S. Kumar, B. Dalela, S. Kumar, P.A. Alvi, S. Dalela, Defects and oxygen vacancies tailored structural and optical properties in CeO₂ nanoparticles doped with Sm³⁺ cation, *J. Alloys Compd.* 752 (2018) 520–531, <https://doi.org/10.1016/j.jallcom.2018.04.157>.
- [31] J.H. Lee, D.Y. Jo, J.W. Choung, C.H. Kim, H.C. Ham, K.Y. Lee, Roles of noble metals (M = Ag, Au, Pd, Pt and Rh) on CeO₂ in enhancing activity toward soot oxidation: Active oxygen species and DFT calculations, *J. Hazard. Mater.* 403 (2021), 124085, <https://doi.org/10.1016/j.jhazmat.2020.124085>.
- [32] Z. Yang, T.K. Woo, K. Hermansson, Effects of Zr doping on stoichiometric and reduced ceria: a first-principles study, *J. Chem. Phys.* 124 (2006), 224704, <https://doi.org/10.1063/1.2200354>.
- [33] H. Wu, S. Ma, W. Song, E.J.M. Hensen, Density Functional Theory Study of the Mechanism of Formaldehyde Oxidation on Mn-Doped Ceria, *J. Phys. Chem. C* 120 (2016) 13071–13077, <https://doi.org/10.1021/acs.jpcc.6b03218>.
- [34] H. Jia, R. Jia, J. Wu, X. Tan, S. Sun, Influence of doping concentration on the elastic properties and electronic structure of the reduced Ce_{1-x}M_xO_{1.785} (M = Ti, Zr) from first principles, *Int. J. Mod. Phys. B* 35 (2021), <https://doi.org/10.1142/s021797922150123x>.
- [35] M. Nolan, J. Fearon, G. Watson, Oxygen vacancy formation and migration in ceria, *Solid State Ion.* 177 (2006) 3069–3074, <https://doi.org/10.1016/j.ssi.2006.07.045>.
- [36] F. Jiang, S. Wang, B. Liu, J. Liu, L. Wang, Y. Xiao, Y. Xu, X. Liu, Insights into the Influence of CeO₂ Crystal Facet on CO₂ Hydrogenation to Methanol over Pd/CeO₂ Catalysts, *ACS Catal.* 10 (2020) 11493–11509, <https://doi.org/10.1021/acscatal.0c03324>.
- [37] J. Shi, H. Wang, Y. Liu, X. Ren, H. Sun, B. Lv, Rapid microwave-assisted hydrothermal synthesis of CeO₂ octahedra with mixed valence states and their catalytic activity for thermal decomposition of ammonium perchlorate, *Inorg. Chem. Front.* 6 (2019) 1735–1743, <https://doi.org/10.1039/c9qi00362b>.
- [38] M. Krishnan, J.W. Nalaskowski, L.M. Cook, Chemical Mechanical Planarization: Slurry Chemistry, Materials, and Mechanisms, *Chem. Rev.* 110 (2010) 178–204, <https://doi.org/10.1021/cr900170z>.
- [39] H.S. Lee, H.D. Jeong, D.A. Dornfeld, Semi-empirical material removal rate distribution model for SiO₂ chemical mechanical polishing (CMP) processes, *Precis. Eng.* 37 (2013) 483–490, <https://doi.org/10.1016/j.precisioneng.2012.12.006>.
- [40] M.-H. Oh, R.K. Singh, S. Gupta, S.-B. Cho, Polishing behaviors of single crystalline ceria abrasives on silicon dioxide and silicon nitride CMP, *Microelectron. Eng.* 87 (2010) 2633–2637, <https://doi.org/10.1016/j.mee.2010.07.040>.
- [41] P. Hu, Y. Chen, R. Sun, Y. Chen, Y. Yin, Z. Wang, Synthesis, characterization and frictional wear behavior of ceria hybrid architectures with 111 exposure planes, *Appl. Surf. Sci.* 401 (2017) 100–105, <https://doi.org/10.1016/j.apsusc.2017.01.005>.
- [42] T. Hoshino, Y. Kurata, Y. Terasaki, K. Susa, Mechanism of polishing of SiO₂ films by CeO₂ particles, *J. Non-Cryst. Solids* 283 (1–3) (2001) 129–136, [https://doi.org/10.1016/S0022-3093\(01\)00364-7](https://doi.org/10.1016/S0022-3093(01)00364-7).
- [43] L. Chen, J. Wen, P. Zhang, B. Yu, C. Chen, T. Ma, X. Lu, S.H. Kim, L. Qian, Nanomanufacturing of silicon surface with a single atomic layer precision via mechanochemical reactions, *Nat. Commun.* 9 (2018) 1542, <https://doi.org/10.1038/s41467-018-03930-5>.
- [44] D. Jiang, W. Wang, L. Zhang, Y. Zheng, Z. Wang, Insights into the Surface-Defect Dependence of Photoreactivity over CeO₂ Nanocrystals with Well-Defined Crystal Facets, *ACS Catal.* 5 (2015) 4851–4858, <https://doi.org/10.1021/acscatal.5b01128>.
- [45] C. Yang, J. Yang, X. Duan, G. Hu, Q. Liu, S. Ren, J. Li, M. Kong, Roles of photo-generated holes and oxygen vacancies in enhancing photocatalytic performance over CeO₂ prepared by molten salt method, *Adv. Powder Technol.* 31 (2020) 4072–4081, <https://doi.org/10.1016/j.apt.2020.08.017>.
- [46] L.M. Cook, Chemical processes in glass polishing, *J. Non-Cryst. Solids* 120 (1990) 152–171, [https://doi.org/10.1016/0022-3093\(90\)90200-6](https://doi.org/10.1016/0022-3093(90)90200-6).
- [47] J. Seo, J.W. Lee, J. Moon, W. Sigmund, U. Paik, Role of the surface chemistry of ceria surfaces on silicate adsorption, *ACS Appl. Mater. Interfaces* 6 (2014) 7388–7394, <https://doi.org/10.1021/am500816y>.
- [48] K.K. Myong, J. Byun, M.-J. Choo, H. Kim, J.Y. Kim, T. Lim, J.J. Kim, Direct and quantitative study of ceria-SiO₂ interaction depending on Ce³⁺ concentration for chemical mechanical planarization (CMP) cleaning, *Mater. Sci. Semicond. Process.* 122 (2021), 105500, <https://doi.org/10.1016/j.mssp.2020.105500>.